ACS Energy LETTERS

http://pubs.acs.org/journal/aelccp

Rapidly In Situ Cross-Linked Poly(butylene oxide) Electrolyte Interface Enabling Halide-Based All-Solid-State Lithium Metal Batteries

Jing Luo, Qian Sun, Jianwen Liang, Keegan Adair, Feipeng Zhao, Sixu Deng, Yang Zhao, Ruying Li, Huan Huang, Rong Yang, Shangqian Zhao, Jiantao Wang,* and Xueliang Sun*

Cite This: *ACS Energy Lett.* 2023, 8, 3676−3684

Read Online

ACCESS | Metrics & More | Article Recommendations | Supporting Information

ABSTRACT: **Halide-based solid-state halide electrolytes (SSEs) were recently revived as promising candidates for next-generation all-solid-state batteries due to their superionic conductivity, direct compatibility with high-voltage cathodes, and scalable production. However, the incompatibility between halide SSEs and lithium metal anodes remains a main challenge to achieve high energy density. Herein, we demonstrate a thin cross-linked poly(butylene oxide) solid polymer electrolyte (xPBO SPE) interlayer on the superionic Li_3InCl_6 SSE to enable lithium metal compatibility. A rapid and solvent-free in situ cross-linking process is developed by reaction between a 0.5 s pulse of trimethylaluminum vapor and the hydroxyl terminal groups of poly(butylene oxide). The Li−Li symmetric cells using xPBO-SPE@Li_3InCl_6 demonstrate a highly stable cycling performance over 1100 h and up to 1.0 mA cm^{-2} and 1.0 mAh cm^{-2}. All-solid-state lithium metal battery (ASSLMB) performance with a $LiCoO_2$ cathode is presented. This new rapid cross-linking strategy shall inspire more possibilities for lithium metal anode integration in ASSLMBs.**

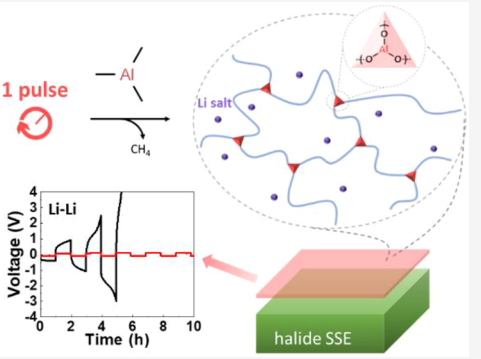

All-solid-state lithium metal batteries (ASSLMBs) are regarded as promising next-generation energy storage systems due to their improved energy density and enhanced safety features compared to the conventional lithium-ion batteries (LIBs) that are based on flammable liquid electrolytes.[1−3] Solid-state electrolytes (SSEs) acting as both the separator and the lithium-ion conductor are key components to the success of ASSLMBs. Recently, studies on halide-based SSEs have been boomingly reviving as a result of the newly demonstrated superionic conductivity above 10^{-4} S cm^{-1} at room temperature and direct compatibility with most layered oxide cathodes.[4−6] The Li-ion conducting chlorides such as $Li_3(Y/Er)Cl_6$[6−10] and Li_2ZrCl_6[11,12] show an ionic conductivity up to 3.1−5.1 × 10^{-4} S cm^{-1}, and even higher room-temperature ionic conductivities of 1.0−3.0 × 10^{-3} S cm^{-1} are reported for Li_3InCl_6,[13,14] Li_xScCl_{3+x} (x = 2.5, 3, 3.5, and 4),[15] $Li_2Sc_{2/3}Cl_4$,[16] $Li_{3-x}(Er/Y)_{1-x}Zr_xCl_6$,[17] $Li_3Y_{1-x}In_xCl_6$,[18] and $Li_{2.25}Zr_{0.75}Fe_{0.25}Cl_6$.[11] These chloride-based SSEs demonstrate intrinsic stability against the favorable oxide cathodes such as $LiCoO_2$ and $LiNi_xMn_yCo_{1-x-y}O_2$ (NMC).[4,19] Moreover, the successful synthesis of superionic Li_3InCl_6 from aqueous solution and an easily scalable process can readily promote the mass production of halide SSEs.[14]

A main drawback of the superionic halide SSEs is their poor electrochemical stability at low voltages and chemical incompatibility against the "holy grail" lithium metal anodes (ultrahigh theoretical specific capacity of 3860 mAh g^{-1}).[3,4,20,21] Construction of a protective layer of solid polymer electrolyte (SPE) on the anode side could be a favorable interfacial engineering strategy,[22−24] but it is challenging to fabricate a thin and mechanically strong SPE film that is compatible with halide SSEs and functional near room temperature. Common cross-linking methods including UV curing,[25−28] chemical cross-linking,[29−31] thermocuring,[32,33] and gamma irradiation[34] can be effective for improving the performance of SPEs, but the often-involved complex preparation procedures, long processing duration, and use of solvent could damage the structure and properties of the superionic halide SSEs.

Received: June 11, 2023
Accepted: August 1, 2023
Published: August 7, 2023

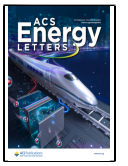

Scheme 1. Rapidly In Situ Cross-Linking Process of the PBO SPE on a Halide SSE Surface

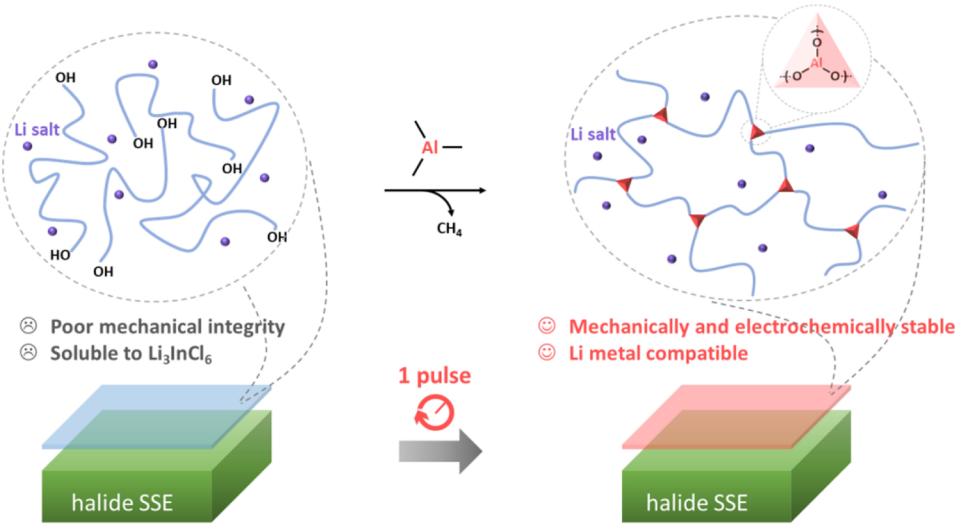

In this work, we propose a vapor-mediated rapid cross-linking method for constructing a cross-linked SPE thin film on the halide SSE surface for good lithium metal compatibility (Scheme 1). Our previously reported near-room-temperature functionable poly(butylene oxide) (PBO)-based SPE is a waxy malleable solid at room temperature.[35] A thin layer of PBO SPE can be applied onto a substrate (e.g., Cu foil or a halide SSE pellet) by a doctor-blade method. In a vacuum chamber at 65 °C, introducing one 0.5 s pulse of trimethylaluminum (TMA) vapor followed by the removal of excess TMA and gaseous byproducts by vacuum can readily lead to a cross-linked xPBO SPE thin film. The TMA reagent is volatile at room temperature and is frequently used in the molecular layer deposition process of organic "alucone" via layer-by-layer condensation polymerization with glycols or diols,[36−39] but TMA has not been reported to enable cross-linking of SPEs to our best knowledge. Presumably, TMA reacts with the hydroxyl terminal groups of the PBO polymer to form a cross-linked network with Al−O joints.

Figure 1a shows the Raman spectrum of the xPBO film in comparison to those of the crystalline PBO at room temperature and the molten PBO at 70 °C. The sharp Raman bands for the crystalline PBO at 1147.2, 1288.4, 1452.6, and 1491.0 cm^{-1} were attributed to the skeletal stretching and the CH_2 wagging and bending modes.[35,40] At molten state, the additional broaden Raman features (marked by gray shading) indicated the increase in disorder (e.g., amorphous state) due to breakdown of the Raman selection rules and an altered phonon density of states.[41,42] The highly similar Raman spectrum of the xPBO to that of the molten PBO suggested a crystalline-to-amorphous transformation in the PBO polymer network. Presumably, the Al-cross-linkers interrupted the crystalline stacking of the planar zigzag PBO chains and facilitated the amorphization of the xPBO network.[40,43] In addition, the solvation behavior of the bis(trifluoromethanesulfonyl)imide lithium salt (LiTFSI) in the SPEs before and after cross-linking can be revealed by the Raman modes of the $TFSI^-$ anions near 746 cm^{-1} (Figure 1b). Deconvolution of this band identified signals from the weakly associated ion pairs at 746.1 cm^{-1} and the free ions at 741.2 cm^{-1}.[44−46] The ratios between the ion pairs and the free ions in the pristine PBO SPE and the xPBO SPE were essentially similar, indicating the unaffected ion association/solvation by the cross-linking process.

The local chemistry at the Al−O cross-linking sites was studied by X-ray absorption near edge structure (XANES). Figure 1c shows the Al K-edge XANES spectra that probed the transitions from the 1s core state to the unoccupied Al-3p-derived states (which should have hybridized with the O 2p states from the PBO terminals) and is sensitive to the oxidation states and bonding environment of Al.[47,48] The Al K-edge spectra of the xPBO and the xPBO SPE samples were consistent in both the edge position and the line shape, suggesting highly similar cross-linking chemistry around the Al-cross-linker despite the presence of LiTFSI salt in the xPBO SPE. The similar absorption edge positions to that of the reference $LiAlO_2$ (~1560.4 eV) indicated an oxidation state of +3 for the Al element in xPBO and the xPBO SPE. In addition, the O K-edge XANES was expected to offer complementary information about the Al−O cross-linking chemistry. Figures 1d and S1 show the O K-edge XANES spectra of the xPBO and the xPBO SPE in comparison with the spectra of pure PBO polymer, un-cross-linked PBO SPE, $LiAlO_2$, and LiTFSI. The O K-edge XANES reflected transitions of O 1s to the unoccupied 2p-derived states.[49] The peak-I at ~533.6 eV and the peak-II at ~537.9 eV corresponded to the pre-edge and whiteline 1s → σ^* transitions.[50−53] Compared to the spectra of PBO and PBO SPE, a decrease in the transition intensity of peak-I, broadening of peak-II, and occurrence of a new high-energy feature marked as peak-III were observed in the spectra of xPBO and xPBO SPE, attributed to the formation of Al−O bonding.

The chemical distribution of the xPBO SPE across the depth of the film was further investigated via time-of-flight secondary ion mass spectrometry (ToF-SIMS). Figure 1e shows the ToF-SIMS depth profiles of C_2H^- (from the PBO backbone), AlC_2O^- and AlO_2^- (indicating the occurrence of the Al−O cross-linking sites), SO^- (from the LiTFSI salt), and Cu^- (substrate) species for xPBO SPE on a Cu foil substrate. Relatively constant counts of C_2H^-, AlC_2O^-, AlO_2^-, and SO^- species were observed over the initial ~400 s of sputtering, followed by a consistent fading of these species and an abrupt increase in counts for the substrate. The temporary irregular response approaching the substrate might be due to the thin

https://doi.org/10.1021/acsenergylett.3c01157
ACS Energy Lett. 2023, 8, 3676−3684

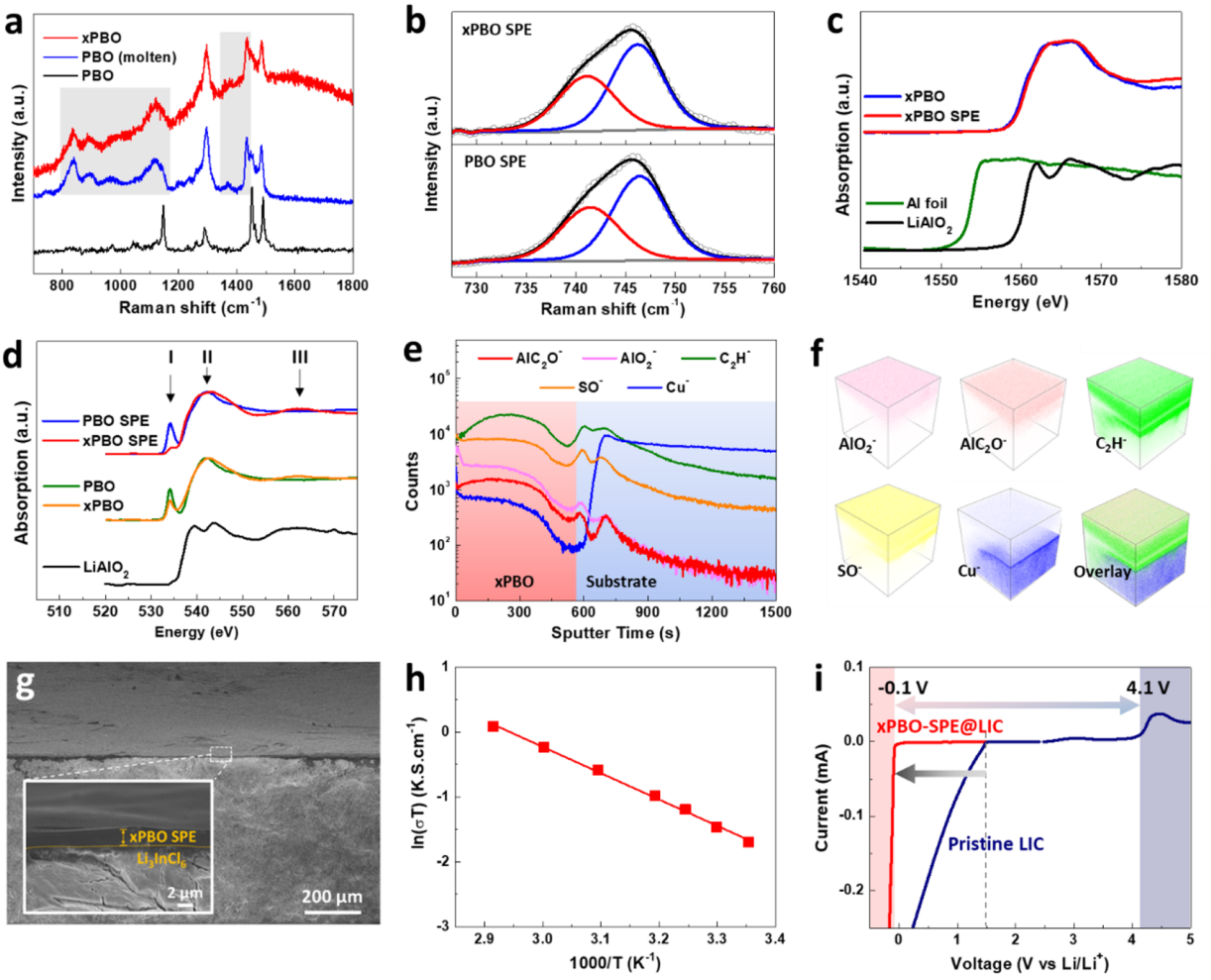

Figure 1. Characterization for the cross-linking chemistry. (a) Raman spectra of xPBO, molten PBO, and pristine crystalline PBO polymers. (b) Raman spectra in the region of $TFSI^-$ modes for PBO SPE before and after cross-linking; Voigt fitting set where the black curve represents the sum of the two fitted functions for the free ion position at 740 cm^{-1} and the contact ion pair position at 746 cm^{-1}, respectively. (c) Al K-edge XANES spectra of xPBO polymer and xPBO SPE in comparison to the reference spectra of Al foil and $LiAlO_2$. (d) O K-edge XANES spectra of xPBO polymer and xPBO SPE in reference to the spectra for pure PBO polymer, un-cross-linked PBO SPE, and $LiAlO_2$. (e) TOF-SIMS depth profiles of AlC_2O^-, AlO_2^-, C_2H^-, SO^-, and Cu^- for xPBO deposited on a Cu foil substrate. (f) Corresponding three-dimensional images of the sputtered volume for the individual species and their overlay. (g) Cross-sectional SEM image of xPBO-SPE@Li_3InCl_6 with a magnified view in the inset. (h) Arrhenius plot of xPBO-SPE@Li_3InCl_6. (i) Extended electrochemical stability window of xPBO-SPE@Li_3InCl_6 compared to that of pristine Li_3InCl_6.

native oxide layer on the surface of Cu foil.[54] The three-dimensional rendered images depicted the uniform distributions of the Al−O cross-linking sites, the PBO backbone, and the dissolved LiTFSI salt across the depth of the xPBO SPE film (Figure 1f).

Considering the large-scale production viability, high ionic conductivity, and direct compatibility with oxide cathodes, the water-mediated synthesized Li_3InCl_6 was chosen as the halide SSE base for interfacial modification.[14] As shown in Figure 1g, a smooth xPBO SPE thin film was constructed on the Li_3InCl_6 surface, namely xPBO-SPE@Li_3InCl_6. The xPBO-SPE thin film was approximately 2 μm in thickness, which was the thinnest we could achieve based on the current coating method. Uniform distributions of Al and C elements on top of an In- and Cl-containing layer were confirmed by energy dispersive X-ray (EDX, Figure S2) analysis. The interfacial engineered xPBO-SPE@Li_3InCl_6 SSE demonstrated an adequate room-temperature ionic conductivity 6.2×10^{-4} S cm^{-1} with an activation energy of 0.350 eV (Figure 1h). Reducing the thickness of the xPBO SPE by incorporating additional advanced coating techniques is expected to further increase the overall ionic conductivity. More importantly, as shown in Figure 1i, the xPBO SPE interlayer was able to significantly extend the onset reduction potential from 1.5 V for Li_3InCl_6 (due to SSE decomposition) to below 0 V for xPBO-SPE@Li_3InCl_6 (lithium deposition). Notably, the protection for Li_3InCl_6 against reduction can be more challenging than for other halide SSEs because of its higher onset reduction potential (e.g., 0.62 V for Li_3YCl_6 vs 2.38 V for Li_3InCl_6 based on first-principles computation[20]). As the xPBO SPE interface is proven effective in protecting Li_3InCl_6 against a lithium metal anode, the strategy should be versatile to other halide SSEs.

The interfacial chemical stability was investigated by temporal electrochemical impedance spectroscopy (EIS) of symmetric cells with lithium metal electrodes and Li_3InCl_6 SSE with or without modification (Figure 2a−c). The high-frequency response (typically above 0.7 MHz) was related to

https://doi.org/10.1021/acsenergylett.3c01157
ACS Energy Lett. 2023, 8, 3676−3684

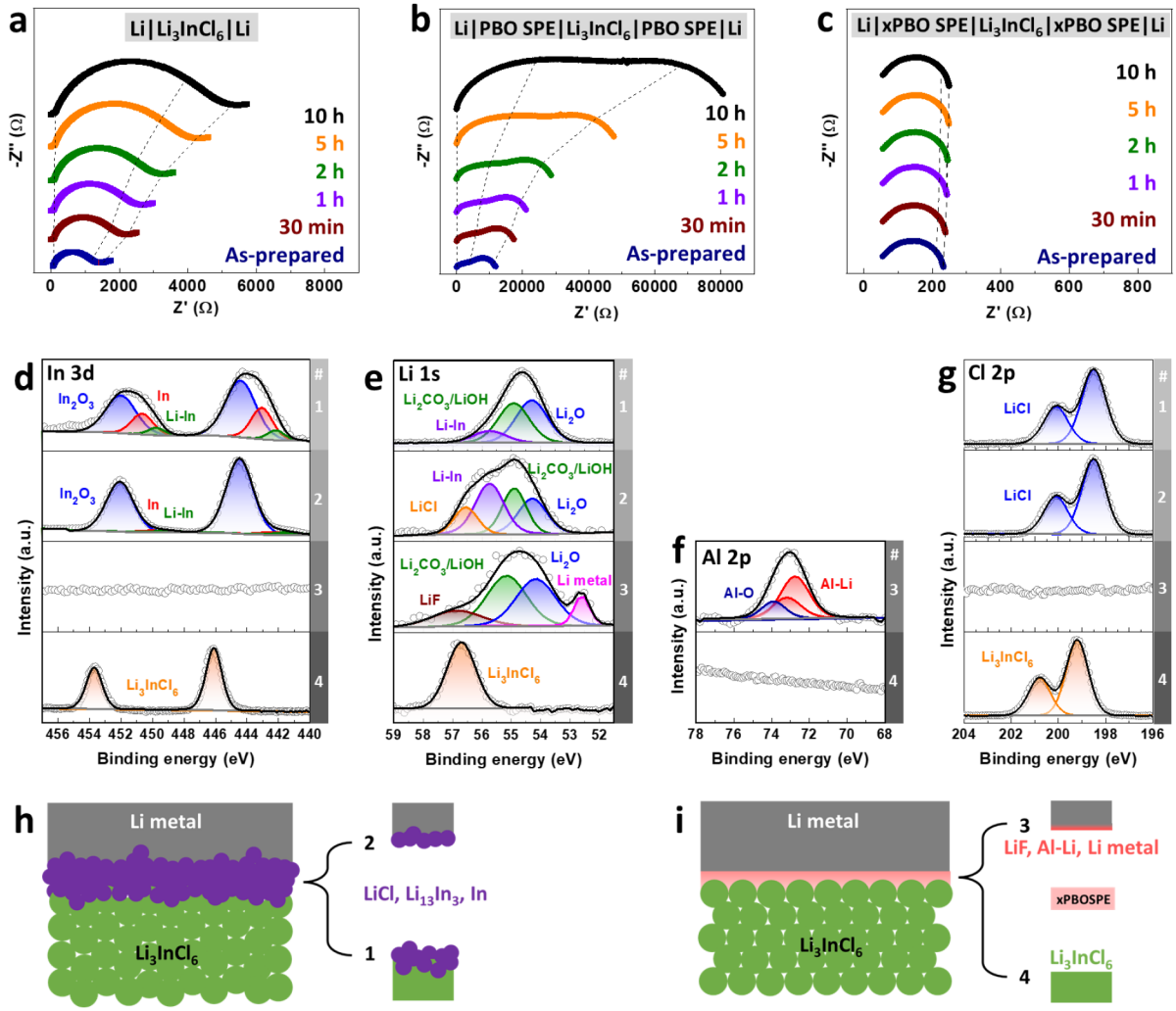

Figure 2. Interfacial characterization. Temporal EIS spectra of Li−Li symmetric cells using (a) unprotected Li_3InCl_6, (b) Li_3InCl_6 with PBO SPE at the interface, and (c) two-sided xPBO-SPE@Li_3InCl_6 as the SSE layer during resting at an open circuit; in a−c, the dashed lines from left to right indicated frequency isolines of 0.7 MHz, 1 kHz, and 10 Hz (the isolines of 1 kHz and 10 Hz almost overlapped in c). XPS spectra of (d) In 3d, (e) Li 1s, (f) Al 2p, and (g) Cl 2p for the surface of lithium metal electrodes or Li_3InCl_6 pellets after integration (contacted or cycled). The corresponding interfaces (#1−4) are schematically illustrated in h and i. (h) Severe degradation of Li_3InCl_6 and lithium metal at the interface. (i) Successful protection of both Li_3InCl_6 and lithium metal by the xPBO SPE interlayer.

the bulk conduction of Li_3InCl_6, while the medium-frequency response (~10^5−10^3 Hz) can be attributed to the Li-ion transport across the interphase/interface between Li metal and Li_3InCl_6 SSE. Figure 2a shows an enlarging medium-frequency response for the cell with unprotected Li_3InCl_6 SSE, suggesting continuous parasitic chemical reactions between the Li metal and Li_3InCl_6 SSE upon aging.[21,55] Notably, a significant medium-frequency semicircle was readily observable for the as-prepared cell, indicating the serious chemical reactions between lithium metal and Li_3InCl_6 had occurred instantly upon contact when the cell was assembled. Unfortunately, after applying the un-cross-linked PBO SPE in between Li_3InCl_6 and lithium metal, the interfacial issue exacerbated (Figure 2b). The drastically enlarging semicircles in the medium- and low-frequency ranges were probably caused by a complex process involving (i) deformation of the waxy PBO SPE under pressure and partial contact between lithium metal and Li_3InCl_6, (ii) degradation of the superionic Li_3InCl_6 due to interfacial dissolution into the PBO SPE (Figure S3),[56,57] and (iii) instability between lithium metal and the untreated hydroxyl terminals of the PBO polymer.[58] Comparatively, Figure 2c shows highly stable EIS aging results for the Li−Li symmetric cell by using xPBO-SPE@Li_3InCl_6. The evolution of medium- and low-frequency semicircles was absent, suggesting successful protection of both the lithium metal electrode and the Li_3InCl_6 SSE by the robust xPBO SPE thin film. The cross-linking process not only had strengthened the mechanical properties of the xPBO SPE to avoid physical deformation and mixing with the Li_3InCl_6 interface but also eliminated the concerning hydroxyl terminals of PBO to improve stability with lithium metal.

To further understand the effectiveness of the protective interlayer of xPBO SPE, the interfacial chemical compositions at the lithium metal side and the Li_3InCl_6 side were characterized by X-ray photoelectron spectroscopy (XPS) after cycling. In addition to the visual differences (Figure S4); the XPS spectra of In 3d, Li 1s, Al 2p, and Cl 2p for the different interfaces are shown in Figure 2d−g, respectively. For the unprotected cell, no matter on the Li_3InCl_6 side or the lithium metal side (Figure 2h), reduction of In^{3+} to In−Li alloy

https://doi.org/10.1021/acsenergylett.3c01157
ACS Energy Lett. 2023, 8, 3676−3684

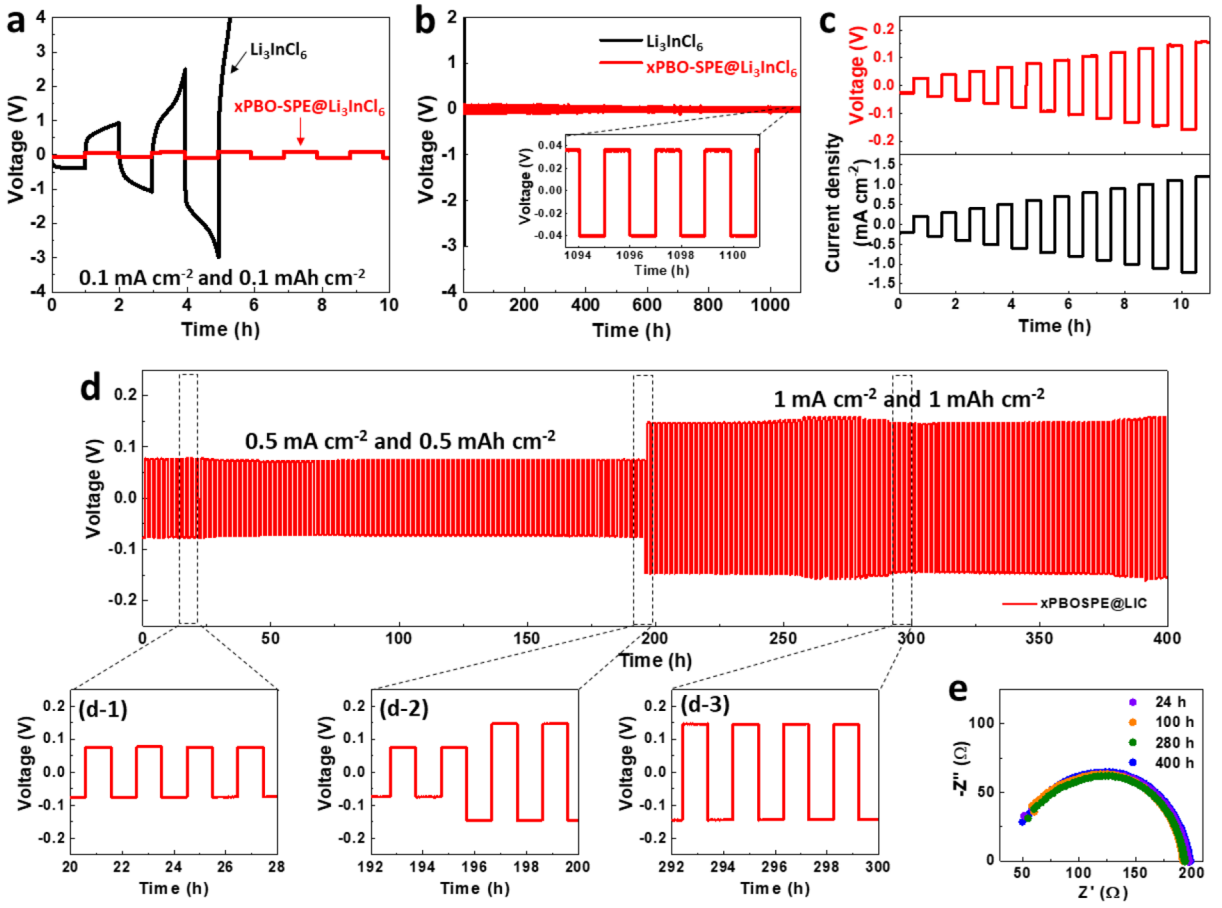

Figure 3. Electrochemical stability of xPBO-SPE@Li_3InCl_6 in Li−Li symmetric cells. (a) Comparison between the Li_3InCl_6 cell and the xPBO-SPE@Li_3InCl_6 cell at 0.1 mA cm^{-2} and 0.1 mAh cm^{-2}. (b) Long cycling of the xPBO-SPE@Li_3InCl_6 cell over 1100 h. (c) Critical current density testing from 0.2 to 1.2 mA cm^{-2}. (d) Cycling performance at higher current densities and capacities. (e) Corresponding EIS spectra during cycling. The cycling tests were conducted at 30 °C.

(i.e., $Li_{13}In_3$ at 442.2 eV for In $3d_{5/2}$ and 55.7 eV for Li 1s) and In metal (443.1 eV for In $3d_{5/2}$) (Figures 2d and S5) were observed along with the formation of LiCl (198.5 eV for Cl $2p_{3/2}$, Figure 2g).[21,55,59−61] Other derived species such as In_2O_3 (444.5 eV for In $3d_{5/2}$), Li_2CO_3/LiOH (55.0 eV for Li 1s), and Li_2O (54.3 eV for Li 1s) were probably due to the surface contamination by the residual oxygen in the measurement chamber.[21] In comparison, the Li_3InCl_6 interface from the xPBO-SPE@Li_3InCl_6 cell maintained pure characteristics of Li_3InCl_6, showing In $3d_{5/2}$ at 446.1, Li 1s at 56.8 eV, and Cl $2p_{3/2}$ at 199.2 eV with no sign of Al interdiffusion from the xPBO SPE layer (Figures 2d−g and S6).[13,21] On the lithium metal side, the absence of In and Cl signals also confirmed the successful physical protection of the xPBO SPE against Li_3InCl_6 penetration and contact. Additionally, a thin interphase consisting of beneficial components such as LiF and Al−Li alloy should have been formed in situ on the lithium metal surface due to minor electrochemical decomposition of the LiTFSI salt and the Al-cross-linked xPBO SPE at the interface. Compared to the symmetric Al 2p peak at 73.8 eV indicative of oxide for the as-prepared xPBO-SPE@Li_3InCl_6 (Figure S7), the asymmetric Al 2p peak and the shift to lower binding energy for the cycled lithium metal interface evidenced the formation of metallic Al/Al−Li alloy (72.8 eV for Al $2p_{3/2}$).[62−64] Moreover, as the average depth of analysis for an XPS measurement is approximately a few nanometers, the observable signal for lithium metal (52.7 eV for Li 1s) suggested that the in situ formed LiF/Al−Li interphase should be very thin.[61] As a conclusion, the robust xPBO SPE protective interlayer was achieved to preserve the superionic Li_3InCl_6 interface while ensuring a favorable lithium metal interface (Figure 2i).

The electrochemical stability of xPBO-SPE@Li_3InCl_6 with a lithium metal electrode was evaluated in Li−Li symmetric cells. Figure 3a compares the cycling stability of Li−Li symmetric cells using unprotected Li_3InCl_6 or the proposed xPBO-SPE@Li_3InCl_6 as the SSE layer. At a low current density of 0.1 mA cm^{-2} and a low areal capacity of 0.1 mAh cm^{-2}, the cell using Li_3InCl_6 readily failed in a few cycles with a rapidly increasing overpotential, indicating severe side reactions between Li_3InCl_6 and lithium metal. In contrast, as shown in Figure 3b, the xPBO-SPE@Li_3InCl_6 cell showed a stable cycling performance with flat lithiation−delithiation overpotential profiles. The slightly reduced overpotential over time can be attributed to the gradual stabilization of the lithium metal surface. Over 1100 h of cycling, the xPBO-SPE@Li_3InCl_6 cell still maintained a low overpotential of ∼40 mV, indicating superior stability and low resistance with the lithium metal electrode. Notably, the salt concentration in the initial PBO SPE can be important in minimizing interfacial Li_3InCl_6 dissolution and subsequent stabilization of the lithium metal surface (Figure S8).

https://doi.org/10.1021/acsenergylett.3c01157
ACS Energy Lett. 2023, 8, 3676−3684

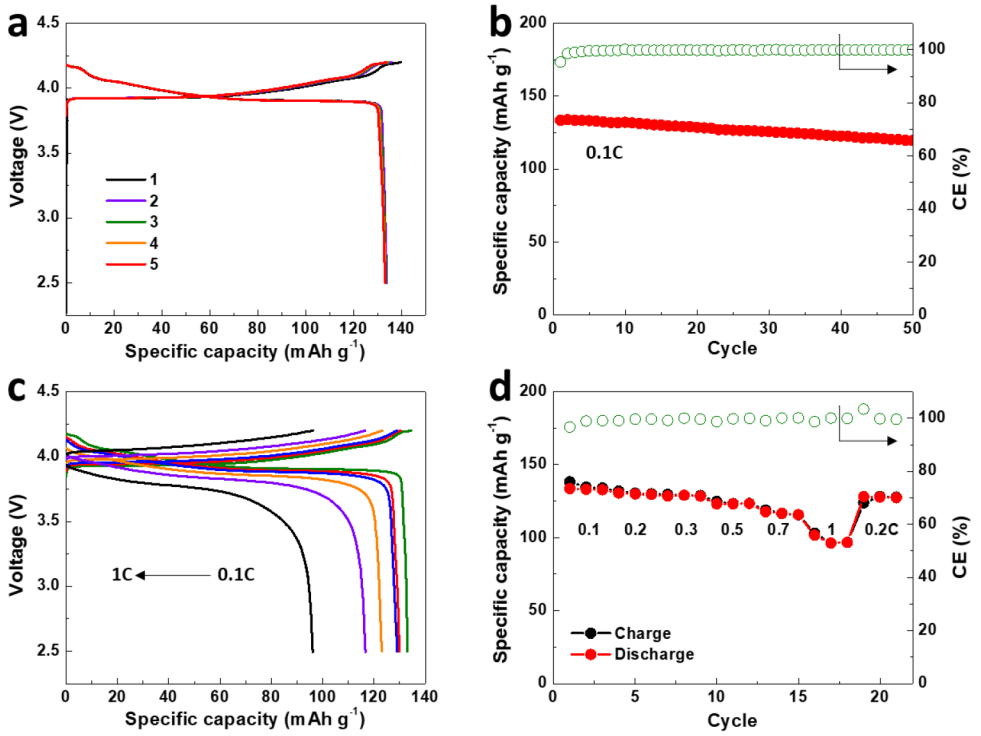

Figure 4. Electrochemical performance of ASSLMBs with a configuration of $LiCoO_2$−Li_3InCl_6|Li_3InCl_6|xPBO SPE|Li. (a) Charge−discharge curves and (b) cycling performance at 0.1 C at 30 °C. (c) Charge−discharge curves and (d) rate performance at different current rates of 0.1, 0.2, 0.3, 0.5, 0.7, and 1 C at 30 °C. The operating voltage window was 2.5 to 4.2 V vs Li^+/Li.

The tolerance of current density and capacity loading was evaluated by incremental current densities with a fixed cycling period of 1 h per cycle (i.e., 0.5 h per lithiation or delithiation process). As shown in Figure 3c, the Li−Li symmetric cell using xPBO-SPE@Li_3InCl_6 demonstrated stable performance up to a high current density of 1.2 mA cm^{-2}. The overpotential increased stepwise, obeying Ohm's law. Upon repeating cycles at higher current densities and higher capacity loadings, highly stable cycling performance was still observed at 0.5 mA cm^{-2} and 0.5 mAh cm^{-2} as well as 1 mA cm^{-2} and 1 mAh cm^{-2} for 200 h at each cycling condition (Figure 3d). As shown in the enlarged voltage profiles during cycling, the lithium deposition/stripping overpotential plateaus were flat and stable, showing no sign of lithium dendrite formation, parasitic side reactions, short circuit, or any other failure modes. The EIS spectra measured at different cycles almost overlapped (Figure 3e), which indicated the essentially unchanged overall cell resistance upon cycling, as consistent with the highly stable lithiation/delithiation overpotential profiles.

Proof-of-concept ASSLMBs based on a $LiCoO_2$ cathode, a Li_3InCl_6 SSE with an in situ prepared xPBO-SPE interlayer on the anode side, and a lithium metal anode were fabricated for battery performance evaluation. Notably, because of the high oxidation stability of Li_3InCl_6, the $LiCoO_2$ cathode particles were directly integrated with the Li_3InCl_6 SSE as received without additional surface coating. Figure 4a shows the initial charge−discharge curves of the ASSLMB at 0.1 C. The initial discharge capacity was 133.4 mAh g^{-1} with a high Coulombic efficiency (CE) of 95.4%. The highly overlapped charge−discharge curves indicated good stability of all interfaces, including $LiCoO_2$/Li_3InCl_6, Li_3InCl_6/xPBO SPE, and xPBO SPE/Li within the ASSLMB. After 50 cycles, a capacity of 119.6 mAh g^{-1} was maintained with a high average CE of 99.8% excluding the initial cycle (Figure 4b). Upon charging and discharging at different current rates, the ASSLMB demonstrated stabilized discharge capacities of 129.9, 129.0, 123.1, 116.7, and 96.2 mAh g^{-1} at 0.2, 0.3, 0.5, 0.7, and 1 C (Figure 4c,d). After returning to 0.2 C from high rates, a discharge capacity of 128.0 mAh g^{-1} returned to the previous level, confirming the excellent stability of the electrode-tailored xPBO-SPE@Li_3InCl_6 SSE to both the 4 V class $LiCoO_2$ cathode (by Li_3InCl_6) and the lithium metal anode (by xPBO SPE). In comparison, a control cell without the xPBO SPE protective interface was not rechargeable due to severe Li_3InCl_6 decomposition at the anode side (Figure S9). The cycling stability and rate capability of the xPBO-SPE@Li_3InCl_6-based ASSLMBs in this work have outperformed other similar halide-based ASSLMBs that had recently been reported for high lithium metal compatibility (Figure S10).[55,65]

In summary, we have demonstrated a novel and effective approach to fabricate a thin in situ cross-linked xPBO SPE interlayer via an instant treatment with TMA vapor. The rapid, solvent-free, and thorough cross-linking process can be easily adaptive for large-scale production. The Al−O cross-linking chemistry not only strengthens the mechanical properties of xPBO SPE but also consumes the unstable hydroxyl terminals of PBO without affecting the lithium-ion solvation in the xPBO SPE. As a result, Li−Li symmetric cells exhibited highly stable deposition/stripping cycling performance; ASSLMBs based on $LiCoO_2$, xPBO-SPE@Li_3InCl_6, and a lithium metal anode demonstrated stable cycling performance and good rate capability. As the xPBO SPE interface ensures lithium metal compatibility for the challenging Li_3InCl_6 (which has the highest reduction onset potential among the reported superionic halide SSEs), this facile protection strategy should be versatile to other halide superionic SSEs with lower

https://doi.org/10.1021/acsenergylett.3c01157
ACS Energy Lett. 2023, 8, 3676−3684

reduction onset potentials and other types of SSEs that are incompatible with lithium metal and sensitive to aqueous/organic solvents, such as sulfide SSEs. In addition to TMA, other metal−organic compounds such as diethylzinc, zirconium tetra-*tert*-butoxide, tetrakis(dimethylamido)titanium, tetrakis(dimethylamido)hafnium, and tetrakis-(ethylmethylamino)vanadium can possibly be used individually or in combination as Zn-, Zr-, Ti-, Hf-, and V-cross-linkers for SPEs to explore additional tunable benefits. This new rapid cross-linking strategy shall also inspire more possibilities for hybrid SSE fabrication and lithium metal anode integration for ASSLMBs.

■ ASSOCIATED CONTENT

Supporting Information

The Supporting Information is available free of charge at https://pubs.acs.org/doi/10.1021/acsenergylett.3c01157.

Experimental methods, additional O K-edge XANES spectra, SEM image and EDX mapping, Raman spectra, XPS results, and comparison of ASSLMB performance (PDF)

■ AUTHOR INFORMATION

Corresponding Authors

Jiantao Wang − *China Automotive Battery Research Institute Co. Ltd, Beijing 100088, China*; Email: wangjt@glabat.com

Xueliang Sun − *Department of Mechanical and Materials Engineering, University of Western Ontario, London, Ontario N6A 5B9, Canada*; orcid.org/0000-0003-0374-1245; Email: xsun9@uwo.ca

Authors

Jing Luo − *Department of Mechanical and Materials Engineering, University of Western Ontario, London, Ontario N6A 5B9, Canada*

Qian Sun − *Department of Mechanical and Materials Engineering, University of Western Ontario, London, Ontario N6A 5B9, Canada*

Jianwen Liang − *Department of Mechanical and Materials Engineering, University of Western Ontario, London, Ontario N6A 5B9, Canada*; orcid.org/0000-0003-4055-1301

Keegan Adair − *Department of Mechanical and Materials Engineering, University of Western Ontario, London, Ontario N6A 5B9, Canada*

Feipeng Zhao − *Department of Mechanical and Materials Engineering, University of Western Ontario, London, Ontario N6A 5B9, Canada*

Sixu Deng − *Department of Mechanical and Materials Engineering, University of Western Ontario, London, Ontario N6A 5B9, Canada*; orcid.org/0000-0001-7458-0296

Yang Zhao − *Department of Mechanical and Materials Engineering, University of Western Ontario, London, Ontario N6A 5B9, Canada*; orcid.org/0000-0002-4148-2603

Ruying Li − *Department of Mechanical and Materials Engineering, University of Western Ontario, London, Ontario N6A 5B9, Canada*

Huan Huang − *Glabat Solid-State Battery Inc., London, ON N6G 4X8, Canada*

Rong Yang − *China Automotive Battery Research Institute Co. Ltd, Beijing 100088, China*

Shangqian Zhao − *China Automotive Battery Research Institute Co. Ltd, Beijing 100088, China*

Complete contact information is available at: https://pubs.acs.org/10.1021/acsenergylett.3c01157

Notes

The authors declare no competing financial interest.

■ ACKNOWLEDGMENTS

This research was supported by Natural Sciences and Engineering Research Council of Canada (NSERC), GLABAT Solid-State Battery Inc., China Automotive Battery Research Institute Co. Ltd, Canada Research Chair Program (CRC), Canada Foundation for Innovation (CFI), Ontario Research Fund, Canada MITACS, Canadian Light Source (CLS), and University of Western Ontario.

■ REFERENCES

(1) Chen, R. J.; Qu, W. J.; Guo, X.; Li, L.; Wu, F. The pursuit of solid-state electrolytes for lithium batteries: from comprehensive insight to emerging horizons. *Mater. Horiz.* **2016**, *3* (6), 487−516.

(2) Cheng, X.-B.; Zhao, C.-Z.; Yao, Y.-X.; Liu, H.; Zhang, Q. Recent Advances in Energy Chemistry between Solid-State Electrolyte and Safe Lithium-Metal Anodes. *Chem.* **2019**, *5* (1), 74−96.

(3) Janek, J.; Zeier, W. G. A solid future for battery development. *Nat. Energy* **2016**, *1* (9), 16141.

(4) Li, X.; liang, j.; Yang, X.; Adair, K.; Wang, C.; Zhao, F.; Sun, X. Progress and Perspectives of Halide-based Lithium Conductors for All-Solid-State Batteries. *Energy Environ. Sci.* **2020**, *13*, 1429−1461.

(5) Liang, J.; Li, X.; Adair, K. R.; Sun, X. Metal Halide Superionic Conductors for All-Solid-State Batteries. *Acc. Chem. Res.* **2021**, *54* (4), 1023−1033.

(6) Asano, T.; Sakai, A.; Ouchi, S.; Sakaida, M.; Miyazaki, A.; Hasegawa, S. Solid Halide Electrolytes with High Lithium-Ion Conductivity for Application in 4 V Class Bulk-Type All-Solid-State Batteries. *Adv. Mater.* **2018**, *30* (44), No. 1803075.

(7) Schlem, R.; Banik, A.; Ohno, S.; Suard, E.; Zeier, W. G. Insights into the Lithium Sub-structure of Superionic Conductors Li3YCl6 and Li3YBr6. *Chem. Mater.* **2021**, *33* (1), 327−337.

(8) Schlem, R.; Muy, S.; Prinz, N.; Banik, A.; Shao-Horn, Y.; Zobel, M.; Zeier, W. G. Mechanochemical Synthesis: A Tool to Tune Cation Site Disorder and Ionic Transport Properties of Li3MCl6 (M = Y, Er) Superionic Conductors. *Adv. Energy Mater.* **2020**, *10* (6), No. 1903719.

(9) Schlem, R.; Bernges, T.; Li, C.; Kraft, M. A.; Minafra, N.; Zeier, W. G. Lattice Dynamical Approach for Finding the Lithium Superionic Conductor Li3ErI6. *ACS Appl. Energy Mater.* **2020**, *3* (4), 3684−3691.

(10) Muy, S.; Voss, J.; Schlem, R.; Koerver, R.; Sedlmaier, S. J.; Maglia, F.; Lamp, P.; Zeier, W. G.; Shao-Horn, Y. High-Throughput Screening of Solid-State Li-Ion Conductors Using Lattice-Dynamics Descriptors. *iScience* **2019**, *16*, 270−282.

(11) Kwak, H.; Han, D.; Lyoo, J.; Park, J.; Jung, S. H.; Han, Y.; Kwon, G.; Kim, H.; Hong, S.-T.; Nam, K.-W.; Jung, Y. S. New Cost-Effective Halide Solid Electrolytes for All-Solid-State Batteries: Mechanochemically Prepared Fe3+-Substituted Li2ZrCl6. *Adv. Energy Mater.* **2021**, *11* (12), No. 2003190.

(12) Wang, K.; Ren, Q.; Gu, Z.; Duan, C.; Wang, J.; Zhu, F.; Fu, Y.; Hao, J.; Zhu, J.; He, L.; Wang, C.-W.; Lu, Y.; Ma, J.; Ma, C. A cost-effective and humidity-tolerant chloride solid electrolyte for lithium batteries. *Nat. Commun.* **2021**, *12* (1), 4410.

(13) Li, X.; Liang, J.; Luo, J.; Norouzi Banis, M.; Wang, C.; Li, W.; Deng, S.; Yu, C.; Zhao, F.; Hu, Y.; Sham, T.-K.; Zhang, L.; Zhao, S.; Lu, S.; Huang, H.; Li, R.; Adair, K. R.; Sun, X. Air-stable Li3InCl6 electrolyte with high voltage compatibility for all-solid-state batteries. *Energy Environ. Sci.* **2019**, *12*, 2665−2671.

(14) Li, X.; Liang, J.; Chen, N.; Luo, J.; Adair, K. R.; Wang, C.; Banis, M. N.; Sham, T.-K.; Zhang, L.; Zhao, S.; Lu, S.; Huang, H.; Li,

R.; Sun, X. Water-Mediated Synthesis of a Superionic Halide Solid Electrolyte. *Angew. Chem., Int. Ed.* **2019**, *58* (46), 16427−16432.
(15) Liang, J.; Li, X.; Wang, S.; Adair, K. R.; Li, W.; Zhao, Y.; Wang, C.; Hu, Y.; Zhang, L.; Zhao, S.; Lu, S.; Huang, H.; Li, R.; Mo, Y.; Sun, X. Site-Occupation-Tuned Superionic LixScCl3+xHalide Solid Electrolytes for All-Solid-State Batteries. *J. Am. Chem. Soc.* **2020**, *142* (15), 7012−7022.
(16) Zhou, L.; Kwok, C. Y.; Shyamsunder, A.; Zhang, Q.; Wu, X.; Nazar, L. F. A new halospinel superionic conductor for high-voltage all solid state lithium batteries. *Energy Environ. Sci.* **2020**, *13*, 2056−2063.
(17) Park, K.-H.; Kaup, K.; Assoud, A.; Zhang, Q.; Wu, X.; Nazar, L. F. High-Voltage Superionic Halide Solid Electrolytes for All-Solid-State Li-Ion Batteries. *ACS Energy Lett.* **2020**, *5*, 533−539.
(18) Li, X.; Liang, J.; Adair, K. R.; Li, J.; Li, W.; Zhao, F.; Hu, Y.; Sham, T.-K.; Zhang, L.; Zhao, S.; Lu, S.; Huang, H.; Li, R.; Chen, N.; Sun, X. Origin of Superionic Li3Y1−xInxCl6 Halide Solid Electrolytes with High Humidity Tolerance. *Nano Lett.* **2020**, *20* (6), 4384−4392.
(19) Kwak, H.; Wang, S.; Park, J.; Liu, Y.; Kim, K. T.; Choi, Y.; Mo, Y.; Jung, Y. S. Emerging Halide Superionic Conductors for All-Solid-State Batteries: Design, Synthesis, and Practical Applications. *ACS Energy Lett.* **2022**, *7*, 1776−1805.
(20) Wang, S.; Bai, Q.; Nolan, A. M.; Liu, Y.; Gong, S.; Sun, Q.; Mo, Y. Lithium Chlorides and Bromides as Promising Solid-State Chemistries for Fast Ion Conductors with Good Electrochemical Stability. *Angew. Chem., Int. Ed.* **2019**, *58* (24), 8039−8043.
(21) Riegger, L. M.; Schlem, R.; Sann, J.; Zeier, W. G.; Janek, J. Lithium-Metal Anode Instability of the Superionic Halide Solid Electrolytes and the Implications for Solid-State Batteries. *Angew. Chem., Int. Ed.* **2021**, *60* (12), 6718−6723.
(22) Li, S.; Lorandi, F.; Wang, H.; Liu, T.; Whitacre, J. F.; Matyjaszewski, K. Functional polymers for lithium metal batteries. *Prog. Polym. Sci.* **2021**, *122*, No. 101453.
(23) Wu, L.; Wang, Y.; Guo, X.; Ding, P.; Lin, Z.; Yu, H. Interface science in polymer-based composite solid electrolytes in lithium metal batteries. *SusMat* **2022**, *2* (3), 264−292.
(24) Ding, P.; Lin, Z.; Guo, X.; Wu, L.; Wang, Y.; Guo, H.; Li, L.; Yu, H. Polymer electrolytes and interfaces in solid-state lithium metal batteries. *Mater. Today* **2021**, *51*, 449−474.
(25) Mackanic, D. G.; Michaels, W.; Lee, M.; Feng, D.; Lopez, J.; Qin, J.; Cui, Y.; Bao, Z. Crosslinked Poly(tetrahydrofuran) as a Loosely Coordinating Polymer Electrolyte. *Adv. Energy Mater.* **2018**, *8* (25), No. 1800703.
(26) Meabe, L.; Huynh, T. V.; Mantione, D.; Porcarelli, L.; Li, C.; O'Dell, L. A.; Sardon, H.; Armand, M.; Forsyth, M.; Mecerreyes, D. UV-cross-linked poly(ethylene oxide carbonate) as free standing solid polymer electrolyte for lithium batteries. *Electrochim. Acta* **2019**, *302*, 414−421.
(27) Zhang, Y.; Lu, W.; Cong, L.; Liu, J.; Sun, L.; Mauger, A.; Julien, C. M.; Xie, H.; Liu, J. Cross-linking network based on Poly(ethylene oxide): Solid polymer electrolyte for room temperature lithium battery. *J. Power Sources* **2019**, *420*, 63−72.
(28) Sutton, P.; Airoldi, M.; Porcarelli, L.; Olmedo-Martínez, J. L.; Mugemana, C.; Bruns, N.; Mecerreyes, D.; Steiner, U.; Gunkel, I. Tuning the Properties of a UV-Polymerized, Cross-Linked Solid Polymer Electrolyte for Lithium Batteries. *Polymer* **2020**, *12* (3), 595.
(29) Khurana, R.; Schaefer, J. L.; Archer, L. A.; Coates, G. W. Suppression of Lithium Dendrite Growth Using Cross-Linked Polyethylene/Poly(ethylene oxide) Electrolytes: A New Approach for Practical Lithium-Metal Polymer Batteries. *J. Am. Chem. Soc.* **2014**, *136* (20), 7395−7402.
(30) Zheng, Q.; Ma, L.; Khurana, R.; Archer, L. A.; Coates, G. W. Structure−property study of cross-linked hydrocarbon/poly(ethylene oxide) electrolytes with superior conductivity and dendrite resistance. *Chem. Sci.* **2016**, *7* (11), 6832−6838.
(31) Huang, S.; Cui, Z.; Qiao, L.; Xu, G.; Zhang, J.; Tang, K.; Liu, X.; Wang, Q.; Zhou, X.; Zhang, B.; Cui, G. An in-situ polymerized solid polymer electrolyte enables excellent interfacial compatibility in lithium batteries. *Electrochim. Acta* **2019**, *299*, 820−827.
(32) Wang, X.; Sun, J.; Feng, C.; Wang, X.; Xu, M.; Sun, J.; Zhang, N.; Ma, J.; Wang, Q.; Zong, C.; Cui, G. Lithium bis(oxalate)borate crosslinked polymer electrolytes for high-performance lithium batteries. *J. Energy Chem.* **2021**, *55*, 228−235.
(33) Borghini, M. C.; Mastragostino, M.; Zanelli, A. Reliability of lithium batteries with crosslinked polymer electrolytes. *Electrochim. Acta* **1996**, *41* (15), 2369−2373.
(34) Mindemark, J.; Sobkowiak, A.; Oltean, G.; Brandell, D.; Gustafsson, T. Mechanical Stabilization of Solid Polymer Electrolytes through Gamma Irradiation. *Electrochim. Acta* **2017**, *230*, 189−195.
(35) Luo, J.; Sun, Q.; Liang, J.; Yang, X.; Liang, J.; Lin, X.; Zhao, F.; Liu, Y.; Huang, H.; Zhang, L.; Zhao, S.; Lu, S.; Li, R.; Sun, X. A liquid-free poly(butylene oxide) electrolyte for near-room-temperature and 4-V class all-solid-state lithium batteries. *Nano Energy* **2021**, *90*, No. 106566.
(36) Dameron, A. A.; Seghete, D.; Burton, B. B.; Davidson, S. D.; Cavanagh, A. S.; Bertrand, J. A.; George, S. M. Molecular Layer Deposition of Alucone Polymer Films Using Trimethylaluminum and Ethylene Glycol. *Chem. Mater.* **2008**, *20* (10), 3315−3326.
(37) Meng, X. An overview of molecular layer deposition for organic and organic−inorganic hybrid materials: mechanisms, growth characteristics, and promising applications. *J. Mater. Chem. A* **2017**, *5* (35), 18326−18378.
(38) Zhao, Y.; Sun, X. Molecular Layer Deposition for Energy Conversion and Storage. *ACS Energy Lett.* **2018**, *3*, 899−914.
(39) George, S. M.; Yoon, B.; Dameron, A. A. Surface Chemistry for Molecular Layer Deposition of Organic and Hybrid Organic-Inorganic Polymers. *Acc. Chem. Res.* **2009**, *42* (4), 498−508.
(40) Matsui, Y.; Kubota, T.; Tadokoro, H.; Yoshihara, T. Raman spectra of polyethers. *J. Polym. Sci., Part A: Gen. Pap.* **1965**, *3* (6), 2275−2288.
(41) Joseph, C.; Bourson, P.; Fontana, M. D. Amorphous to crystalline transformation in Ta2O5 studied by Raman spectroscopy. *J. Raman Spectrosc.* **2012**, *43* (8), 1146−1150.
(42) Zwick, A.; Carles, R. Multiple-order Raman scattering in crystalline and amorphous silicon. *Phys. Rev. B* **1993**, *48* (9), 6024−6032.
(43) Vainshtein, E. F.; Kushnerev, M. Y.; Popov, A. A.; Entelis, S. G. The crystalline structure of polytetrahydrofuran. *Polym. Sci. U.S.S.R.* **1969**, *11* (7), 1820−1825.
(44) Das, S.; Ghosh, A. Structure, ion transport, and relaxation dynamics of polyethylene oxide/poly (vinylidene fluoride co-hexafluoropropylene) - Lithium bis(trifluoromethane sulfonyl) imide blend polymer electrolyte embedded with ionic liquid. *J. Appl. Phys.* **2016**, *119*, 095101.
(45) Edman, L. Ion Association and Ion Solvation Effects at the Crystalline−Amorphous Phase Transition in PEO−LiTFSI. *J. Phys. Chem. B* **2000**, *104* (31), 7254−7258.
(46) Sun, B.; Mindemark, J.; Morozov, E. V.; Costa, L. T.; Bergman, M.; Johansson, P.; Fang, Y.; Furo, I.; Brandell, D. Ion transport in polycarbonate based solid polymer electrolytes: experimental and computational investigations. *Phys. Chem. Chem. Phys.* **2016**, *18* (14), 9504−9513.
(47) Yang, C. K.; Chiou, J. W.; Tsai, H. M.; Pao, C. W.; Jan, J. C.; Ray, S. C.; Yeh, C. L.; Huang, K. C.; Hsueh, H. C.; Pong, W. F.; Tsai, M.-H.; Hsieh, H. H.; Lin, H. J.; Hou, T. Y.; Hsu, J. H. Electronic structure and magnetic properties of Al-doped Fe3O4 films studied by x-ray absorption and magnetic circular dichroism. *Appl. Phys. Lett.* **2005**, *86* (6), No. 062504.
(48) Shimizu, K.-i.; Kato, Y.; Yoshida, H.; Satsuma, A.; Hattori, T.; Yoshida, T. Al K-edge XANES study for the quantification of aluminium coordinations in alumina. *Chem. Commun.* **1999**, *17*, 1681−1682.
(49) Frati, F.; Hunault, M. O. J. Y.; de Groot, F. M. F. Oxygen K-edge X-ray Absorption Spectra. *Chem. Rev.* **2020**, *120* (9), 4056−4110.
(50) Kortright, J. B.; Sun, J.; Spencer, R. K.; Jiang, X.; Zuckermann, R. N. Oxygen K Edge Scattering from Bulk Comb Diblock Copolymer Reveals Extended, Ordered Backbones above Lamellar

https://doi.org/10.1021/acsenergylett.3c01157
ACS Energy Lett. 2023, 8, 3676−3684

Order−Disorder Transition. *J. Phys. Chem. B* **2017**, *121* (1), 298−305.
(51) Aarva, A.; Deringer, V. L.; Sainio, S.; Laurila, T.; Caro, M. A. Understanding X-ray Spectroscopy of Carbonaceous Materials by Combining Experiments, Density Functional Theory, and Machine Learning. Part I: Fingerprint Spectra. *Chem. Mater.* **2019**, *31* (22), 9243−9255.
(52) Dinachandra Singh, M.; Dalvi, A.; Phase, D. M. Electrical transport in PEO-NaI-NASICON nanocomposites: An assessment using impedance and X-Ray absorption spectroscopy. *Mater. Res. Bull.* **2019**, *118*, No. 110485.
(53) Liang, X.; Pan, D.; Lao, M.; Liang, S.; Huang, D.; Zhou, W.; Guo, J. Structural evolution of fluorinated graphene upon molten-alkali treatment probed by X-ray absorption near-edge structure spectroscopy. *Appl. Surf. Sci.* **2017**, *404*, 1−6.
(54) Wang, Z.; Carrière, C.; Seyeux, A.; Zanna, S.; Mercier, D.; Marcus, P. XPS and ToF-SIMS Investigation of Native Oxides and Passive Films Formed on Nickel Alloys Containing Chromium and Molybdenum. *J. Electrochem. Soc.* **2021**, *168* (4), No. 041503.
(55) Wang, C.; Liang, J.; Luo, J.; Liu, J.; Li, X.; Zhao, F.; Li, R.; Huang, H.; Zhao, S.; Zhang, L.; Wang, J.; Sun, X. A universal wet-chemistry synthesis of solid-state halide electrolytes for all-solid-state lithium-metal batteries. *Sci. Adv.* **2021**, *7* (37), No. eabh1896.
(56) Clarke, J. H. R.; Hester, R. E. Vibrational Spectra of Molten Salts. VI. Raman Spectra of Indium Trichloride−Alkali-Metal Chloride Mixtures. *J. Chem. Phys.* **1969**, *50* (7), 3106−3112.
(57) Li, W.; Liang, J.; Li, M.; Adair, K. R.; Li, X.; Hu, Y.; Xiao, Q.; Feng, R.; Li, R.; Zhang, L.; Lu, S.; Huang, H.; Zhao, S.; Sham, T.-K.; Sun, X. Unraveling the Origin of Moisture Stability of Halide Solid-State Electrolytes by In Situ and Operando Synchrotron X-ray Analytical Techniques. *Chem. Mater.* **2020**, *32* (16), 7019−7027.
(58) Yang, X.; Jiang, M.; Gao, X.; Bao, D.; Sun, Q.; Holmes, N.; Duan, H.; Mukherjee, S.; Adair, K.; Zhao, C.; Liang, J.; Li, W.; Li, J.; Liu, Y.; Huang, H.; Zhang, L.; Lu, S.; Lu, Q.; Li, R.; Singh, C. V.; Sun, X. Determining the limiting factor of the electrochemical stability window for PEO-based solid polymer electrolytes: main chain or terminal − OH group? *Energy Environ. Sci.* **2020**, *13* (5), 1318−1325.
(59) Hewitt, R. W.; Winograd, N. Oxidation of polycrystalline indium studied by x-ray photoelectron spectroscopy and static secondary ion mass spectroscopy. *J. Appl. Phys.* **1980**, *51* (5), 2620−2624.
(60) Webb, S. A.; Baggetto, L.; Bridges, C. A.; Veith, G. M. The electrochemical reactions of pure indium with Li and Na: Anomalous electrolyte decomposition, benefits of FEC additive, phase transitions and electrode performance. *J. Power Sources* **2014**, *248*, 1105−1117.
(61) Liang, X.; Pang, Q.; Kochetkov, I. R.; Sempere, M. S.; Huang, H.; Sun, X. Q.; Nazar, L. F. A facile surface chemistry route to a stabilized lithium metal anode. *Nat. Energy* **2017**, *2* (9), 17119.
(62) Oswald, S.; Thoss, F.; Zier, M.; Hoffmann, M.; Jaumann, T.; Herklotz, M.; Nikolowski, K.; Scheiba, F.; Kohl, M.; Giebeler, L.; Mikhailova, D.; Ehrenberg, H. Binding Energy Referencing for XPS in Alkali Metal-Based Battery Materials Research (II): Application to Complex Composite Electrodes. *Batteries* **2018**, *4* (3), 36.
(63) Chen, G.; Weng, Y.; Sun, F.; Zhou, X.; Wu, C.; Yan, Q.; Guo, T.; Zhang, Y. Low-temperature atomic layer deposition of Al2O3/alucone nanolaminates for OLED encapsulation. *RSC Adv.* **2019**, *9* (36), 20884−20891.
(64) Kumar, N.; Biswas, K. Cryomilling: An environment friendly approach of preparation large quantity ultra refined pure aluminium nanoparticles. *J. Mater. Res. Technol.* **2019**, *8* (1), 63−74.
(65) Yu, T.; Liang, J.; Luo, L.; Wang, L.; Zhao, F.; Xu, G.; Bai, X.; Yang, R.; Zhao, S.; Wang, J.; Yu, J.; Sun, X. Superionic Fluorinated Halide Solid Electrolytes for Highly Stable Li-Metal in All-Solid-State Li Batteries. *Adv. Energy Mater.* **2021**, *11* (36), No. 2101915.

https://doi.org/10.1021/acsenergylett.3c01157
ACS Energy Lett. 2023, 8, 3676−3684